



Article

Influence of the Fuel/Oxidant Ratio on the Elaboration of Binary Oxide Catalyst by a Microwave-Assisted Solution Combustion Method

Kawthar Frikha^{1,2,3}, Simona Bennici^{1,2} , Jamel Bouaziz³, Kamel Chaari³ and Lionel Limousy^{1,2,*} 

¹ Institut de Science des Matériaux, CNRS, IS2M UMR 7361, Université de Haute-Alsace, F-68100 Mulhouse, France; kawthar.frikha@uha.fr (K.F.); simona.bennici@uha.fr (S.B.)

² Institut de Science des Matériaux, CNRS, UMR 7361, Université de Strasbourg, 67000 Strasbourg, France

³ Laboratoire de Chimie Industrielle, Département de Génie des Matériaux, Université de Sfax, Ecole Nationale d'Ingénieurs de Sfax, BP 1173, Sfax 3038, Tunisie; jamel.bouaziz@enis.rnu.tn (J.B.); kamel.chaari@enis.rnu.tn (K.C.)

* Correspondence: lionel.limousy@uha.fr; Tel.: +33-389-608-705

Received: 27 April 2020; Accepted: 12 June 2020; Published: 16 June 2020



Abstract: Three series of binary metal oxide catalysts containing Ni, Cu, or Co oxides were prepared, fully characterized and tested in CO oxidation. The catalysts, with a constant transition metal loading of 10 wt%, were prepared from metal nitrates and urea mixtures by a microwave-assisted solution combustion method. The RV/OV ratio, corresponding to the stoichiometry of the reactants, calculated from their elemental oxidizing and reducing valences, was varied. In order to modify the redox character of the synthesis medium from the quantity of urea; an excess of urea was used for attaining reducing conditions, while a deficit of urea shifted the medium to oxidizing conditions. Three RV/OV ratios (0.9, 1.0, and 1.1) were selected to elaborate the different binary metal oxide catalysts, nine oxide catalysts were synthesized. Then, the influence of the stoichiometry (RV/OV ratio) on the bulk and surface properties of the binary metal oxide catalysts was investigated. Similarly, the influence of the RV/OV ratio on the CO oxidation activity was discussed and the optimal value of RV/OV ratio was identified. The results show that the increasing of the RV/OV ratio from 0.9 to 1.1, particularly in Ni- and Co-containing catalysts, induces stronger metal-aluminum interactions, in the form of aluminates phases, and that are correlated to the dramatic reduction of the CO oxidation activity. The best physicochemical properties and highest catalytic activities were achieved with the catalysts prepared in redox systems stoichiometrically balanced (RV/OV = 1). The Cu-containing catalysts presented the best catalytic activities in CO oxidation.

Keywords: Ni; Cu; or Co oxides; CO oxidation; microwave-assisted solution combustion; influence of the stoichiometry

1. Introduction

Metal oxides are among the most useful catalytic materials in heterogeneous redox catalysis. In this category, the active phase can consist of a single metal oxide or a combination of metal oxides. Metal oxide catalysts are applied in a wide range of catalytic reactions, including selective reduction reactions, selective oxidation reactions and total oxidation reactions [1–3]. Transition metal oxides are very interesting in heterogeneous catalysis, due to their improved and tunable acid-base and redox properties [4–7]. Additional assets are the easy availability, the low price, the durability, the regeneration capability, and the resistance to poisoning [8]. The most commonly used transition metal oxide catalysts include chromium oxide, manganese dioxide, iron oxide, cobalt oxide, nickel oxide and

copper oxide [9]. Dispersed on a porous support or mixed with other metal oxides, the combination of two metal oxides presents higher catalytic activity than that of the constituent single oxides [9].

Metal oxide catalysts can be prepared by different methods that drive the structural, textural and surface properties of the solid. The thermal, chemical and mechanical stability of the final solid can be then improved, as well as the catalytic properties. Metal oxides, both simple and complex (bulk and supported), can be synthesized by different routes. The most common methods used are: ceramic method (solid-state reaction), wet chemical methods like co-precipitation, sol-gel and impregnation [10–14]. Even if well established, these conventional methods still present considerable drawbacks as they need a high number of synthetic steps, they are highly energy and time-consuming, and they require specific equipment. Some more recent preparation routes, such as microwave-assisted solution combustion method, have allowed to overcome these disadvantages. The advantages of this method over conventional methods include the very short time duration, the setup simplicity and the high reaction rates [15–23]. The solution combustion (SC) method is based on an exothermic self-sustained redox reaction. It is carried on in a homogeneous aqueous solution containing at least an oxidizing agent and a suitable fuel (used as reducing agent) [24–29]. Salts, like nitrates, metal sulphates and carbonates are chosen as oxidizing agents. Nitrate salts are the preferred metal precursors because they are low temperature oxidizer sources and have great water solubility [30]. Metal nitrates are used at a large scale and considered essential metal precursors for the synthesis of simple and mixed metal oxides. A suitable fuel should have a high solubility in the solvent used (in most cases water), evolve large amounts of harmless gases, be compatible to the oxidizer leading to a controlled combustion, be readily available and non-toxic [30]. Urea is among the most attractive fuels studied for preparing a variety of mixed metal oxides, resulting in the formation of highly thermally stable, pure and homogeneous product, contrary to others fuels that need further thermal treatments after the combustion process at high temperatures to burn away residual impurities.

SC-reaction initiation is achieved through external heating of the reaction mixture up to its ignition temperature. Different electrical heating devices, such as muffle oven, hot plate, aluminum open cylindrical reactor, and pressure reactor [31–36] have been used for supplying the required energy for heating the solution mixture. However, most of these traditional heating processes lead to a thermal gradient between the interior and exterior of the heated solution, resulting in a local inhomogeneity of the prepared material. Unlike conventional heating, microwave (MW) heating provides internal, fast and volumetric heating of the solution, through generation of localized high temperature zones (preferential nucleation sites) in the reaction medium by direct coupling of MW irradiation with the water molecules [17,18]. The ability of microwaves to heat a reaction mixture very rapidly by magnetic dipolar coupling guarantees the homogeneity of the nucleation process [37]. Improved crystal shape, low crystal size and narrow size distributions of the final product are then obtained [38]. Other advantages of microwave heating are the short reaction times, the improved reaction rate and the lower operating temperatures [22,23]. Catalytic materials, whose overall properties are strongly dependent on their synthesis routes, could benefit a great deal from MW heating.

The SC method is based on the thermochemical concepts of propellant chemistry developed by Jain et al. [39]. These concepts contribute to the estimation of the mixture ratio (RV/OV) of fuel-oxidizer compositions. RV/OV ratio can be determined by Equation (1):

$$\frac{RV}{OV} = \frac{\sum \text{Molenumbers of reducing agent} \times \text{reducing valence}}{(-1) \sum \text{Molenumbers of oxidizing agent} \times \text{oxidizing valence}} \quad (1)$$

The oxidizing elements present negative valences, while the reducing elements have positive valences. Metals (positive valence), carbon (valence of +4) and hydrogen (valence of +1) are considered reducing elements. On the other hand, oxygen is considered an oxidizing element with the valence (−2). The elemental valence of nitrogen is zero. Hydration water does not affect the overall system valence, so it is not involved in the RV/OV ratio calculation. The total reducing valence is calculated by adding the elemental reducing and oxidizing valences of the fuel. On the other hand, the total

oxidizing valence is determined by adding the elemental oxidizing and reducing valences of the oxidizer [24,25]. When $RV/OV = 1$, the redox system (fuel-oxidizer mixture) is stoichiometrically balanced, the maximum of energy is released, then ensuring the complete combustion of the fuel. When $RV/OV < 1$, the redox system is in fuel-lean conditions, molecular oxygen is released. In the third case, when $RV/OV > 1$, the redox system is in fuel-rich conditions, and it requires atmospheric oxygen for the complete combustion of the fuel. The thermochemistry of the redox mixture seems to be mainly controlled by the total composition of oxidizing and reducing elements of the mixture [25]. The properties of solution combustion-derived products are strongly influenced by the RV/OV ratio. Generally, any deviation from the stoichiometry balance affects the maximum combustion temperature and the volume of gases generated during the combustion reaction. These two parameters contribute to the tuning of the crystalline phases, the particle size, the morphology, the pore size and volume, the surface area, and the agglomeration degree [26]. Fuel-lean conditions in SC synthesis usually bring to the decrease of the maximum combustion temperature with a consequent reduction of the volume of gases evolved. On the other hand, fuel-rich conditions provoke the increase of the maximum combustion temperature and of the volume of gases generated. A RV/OV value very far from the stoichiometry can lead to an organic-rich and amorphous product, which needs a further calcination step previous to application [24].

In our previous work [40], Ni, Cu, and Co-containing catalysts with metal loading of 10 wt% have been prepared at a unique RV/OV ratio of 1.1 by a microwave-assisted SC method, and tested in carbon monoxide oxidation. In the present study, the aim is to better understand the influence of the RV/OV ratio on the physicochemical properties of binary metal oxide catalysts, prepared by microwave-assisted SC method. The correlation between physicochemical properties of the catalysts and their activity toward CO oxidation is also described. The comparative study of three series of catalysts obtained at different RV/OV ratios allow to make reliable comparisons. Consequently, the optimal synthesis conditions, in terms of RV/OV ratio, can be identified to obtain the desired catalysts' characteristics. Moreover, the use of three different metal oxides provided insights on the influence of the metal nature on the structural and catalytic characteristics of the binary oxide materials.

2. Materials and Methods

2.1. Catalyst Preparation

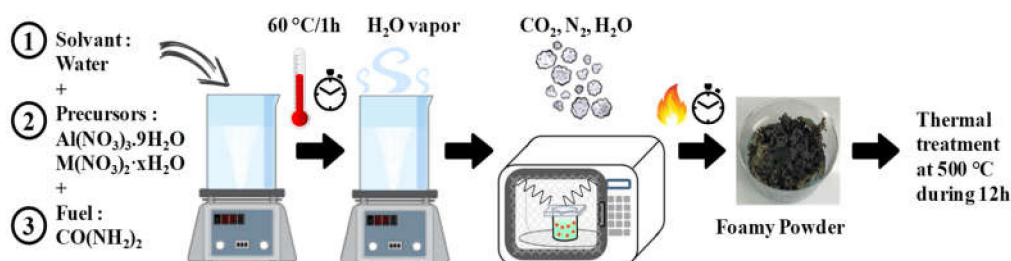
The synthesis of the three series of binary metal oxide catalysts was carried out by microwave-assisted SC method with the same procedure described in a previous work [40]. $Al(NO_3)_3 \cdot 9H_2O$ and $CO(NH_2)_2$ with a purity higher than 98 and 99%, respectively, were purchased from Fluka (Steinheim am Albuch, Baden-Württemberg, Germany). $Cu(NO_3)_2 \cdot 3H_2O$, $Ni(NO_3)_2 \cdot 6H_2O$ and $Co(NO_3)_2 \cdot 6H_2O$ with a purity higher than 99.5%, 99% and 99%, respectively, were purchased from Merck (Darmstadt, Hessen, Germany). These reagents were used as precursors without applying any further purification. The reducing and oxidizing valences as well as the quantities of all the reactants used to elaborate the different catalysts are reported in Table 1.

Table 1. Oxidizing and reducing valences and quantities of the different chemical reagents used to prepare the different catalysts.

Reactant	Elemental Valences	Total Oxidizing Valence	Total Reducing Valence
$\text{Al}(\text{NO}_3)_3 \cdot 9\text{H}_2\text{O}$	1Al = +3; 3N = 0; 9O = -18; 9H ₂ O = 0	-15	-
$\text{Ni}(\text{NO}_3)_2 \cdot 6\text{H}_2\text{O}$	1Ni = +2; 2N = 0; 6O = -12; 6H ₂ O = 0	-10	-
$\text{Co}(\text{NO}_3)_2 \cdot 6\text{H}_2\text{O}$	1Co = +2; 2N = 0; 6O = -12; 6H ₂ O = 0	-10	-
$\text{Cu}(\text{NO}_3)_2 \cdot 3\text{H}_2\text{O}$	1Cu = +2; 2N = 0; 6O = -12; 3H ₂ O = 0	-10	-
$\text{CO}(\text{NH}_2)_2$	1C = +4; 4H = +4; 2N = 0; 1O = -2	-	+6

Weight (g)						
Sample	Water	$\text{Al}(\text{NO}_3)_3 \cdot 9\text{H}_2\text{O}$	$\text{CO}(\text{NH}_2)_2$	$\text{Ni}(\text{NO}_3)_2 \cdot 6\text{H}_2\text{O}$	$\text{Co}(\text{NO}_3)_2 \cdot 6\text{H}_2\text{O}$	$\text{Cu}(\text{NO}_3)_2 \cdot 3\text{H}_2\text{O}$
10NiAl-0.9	10	16	6.135	1.197		
10NiAl-1.0	10	16	6.816	1.197		
10NiAl-1.1	10	16	7.498	1.197		
10CoAl-0.9	10	16	6.133		1.193	
10CoAl-1.0	10	16	6.815		1.193	
10CoAl-1.1	10	16	7.496		1.193	
10CuAl-0.9	10	16	6.106			0.918
10CuAl-1.0	10	16	6.785			0.918
10CuAl-1.1	10	16	7.463			0.918

In a typical experiment, well-defined quantities of aluminum nitrate ($\text{Al}(\text{NO}_3)_3 \cdot 9\text{H}_2\text{O}$) and transition metal nitrate hydrates ($\text{M}(\text{NO}_3)_2 \cdot x\text{H}_2\text{O}$, where M = Ni, Cu or Co; x = 6, 3 or 6, and represents the number of water molecules) were dissolved in 10 mL of demineralized water and stirred for 10 min, as described at Figure 1. Then, adjusted quantities of urea was added to the prepared solution (stirred at 450 rpm), during 1 h at 60 °C, in order to reduce the quantity of water. The solution was then poured into a 50 mL glass beaker and heated in a laboratory microwave oven operating at 700 W, 2.45 GHz. The whole combustion process, for all samples, ended-up in less than 10 min, while the actual time of ignition was shorter than 5 s. The powders were heated in atmospheric air in a muffle furnace at 500 °C for 12 h with a heating rate of 5 °C min⁻¹ to burn away the remaining urea and nitrates and increase the purity of the catalysts. In all cases, the required amount of metal nitrates and urea were adjusted by applying the thermochemical concepts of propellant chemistry [39], and by fixing the RV/OV ratio at 0.9, 1.0 and 1.1. The combustion-synthesized catalysts were labelled as 10MAl-x (where M = Ni, Cu or Co; x = 0.9, 1.0, and 1.1, and represented the RV/OV ratio).

**Figure 1.** Experimental setup used for the synthesis of binary oxide catalysts through microwave-assisted solution combustion.

2.2. Catalyst Characterization

The binary oxide catalysts were characterized by X-ray diffraction (XRD), N₂ adsorption-desorption, scanning electron microscopy (SEM), and X-ray photoelectron spectroscopy (XPS) techniques. Elemental

analyses were carried out by Wavelength Dispersive X-ray Fluorescence (WDXRF) using a Zetium (4 kW) spectrometer (PANalytical, Eindhoven, The Netherlands).

X-ray diffraction (XRD) characterizations were carried out with an X'Pert Pro MPD diffractometer (PANalytical, Eindhoven, The Netherlands) which operates with Cu K α radiation ($\lambda = 0.15406$ nm at 40 mA and 45 k). X-ray patterns were recorded at 20 °C, using 2 theta ($2\theta^\circ$) scanning range from 10 to 90°, and a step size of 0.017° with a scan step time of 220 s. Data processing was then carried out using HighScore software. Phase identification of the materials was made using database cards provided by ICDD.

Nitrogen adsorption-desorption isotherms were recorded at -196 °C using an ASAP2040 apparatus (Micromeritics, Norcross, GA, USA). Prior to measurement, the powders were outgassed under vacuum at 200 °C for 10 h. Determination of physisorption isotherms and associated hysteresis loops was done according to IUPAC classifications. Brunauer-Emmett-Teller (BET) methodology was used to evaluate the surface area of the different materials. Barrett-Joyner-Halenda (BJH) method was used to calculate the pore volume and the average pore diameter of the materials by exploiting the desorption branch of the isotherm.

Scanning electron microscopy (SEM) was performed on an XL30 microscope (PHILIPS, Tokyo, Japan) operating at 7 kV accelerating voltage, while SEM-EDX microanalysis were conducted at 15 kV accelerating voltage. Prior to SEM measurement, the samples were deposited on a flat support covered with a carbon tape, in order to obtain a conductive surface.

Extreme surface characterization was carried out by X-ray photoelectron spectroscopy (XPS). A SES 2002 spectrometer (AVG Scienta, Uppsala, Sweden) equipped with a monochromatic Al K α X-ray radiation source (Al K $\alpha = 1486.6$ eV) was used for these analysis. A high vacuum (10^{-9} Pa) and a pass energy of 100 eV were used during the experimentation. The analyzed zone has a surface of 24 mm² and an analysis depth between 3 and 10 nm depending on the studied material. C 1s peak (284.7 eV) was used as reference to calibrate the binding energies. Gaussian-Lorentzian functions were used to fit XPS peaks with the XPS-CASA software (Version 2.3.18, Teignmouth, UK).

2.3. Catalyst Activity Evaluation

CO oxidation was used as model reaction ($\text{CO} + \frac{1}{2}\text{O}_2 \rightarrow \text{CO}_2$) to compare the catalysts performances according to the RV/OV ratio and the material characteristics. As carbon dioxide is the only product of the reaction, the yield of CO conversion is determined from the percentage of CO converted into CO₂. Measurements of the catalytic activity were conducted in a vertical tubular quartz reactor (internal diameter of 16 mm), using transient (from room temperature to 500 °C) or stationary conditions, for all catalysts. The experimental setup is presented in Figure 2.

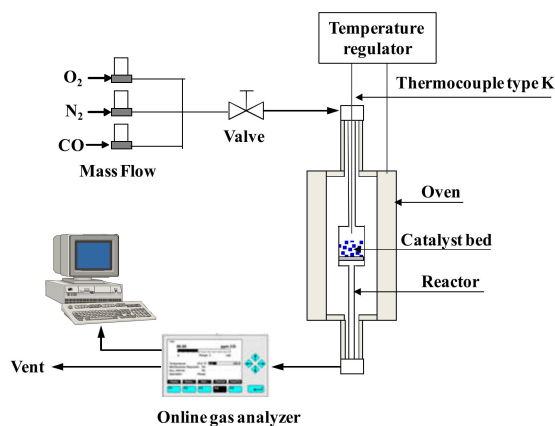


Figure 2. Experimental setup used for the catalytic tests carried out with the different binary metal oxide materials.

Catalyst particles with a 40–60 mesh size were used to fill the reactor. Then, the reactor was introduced in a vertical electric tubular oven, the desired temperature was reached at a range of $5\text{ }^{\circ}\text{C min}^{-1}$ at atmospheric pressure under nitrogen (50 NLh^{-1}). During the catalytic experiments, CO concentration was 0.05 vol%, O_2 1 vol% in N_2 . A constant gas flow rate was maintained at 50 NLh^{-1} during the experiments. The space velocity (GHSV) was fixed at $3500\text{ mLg}_{\text{cat}}^{-1}\text{h}^{-1}$. Numerical mass flowmeters (Brooks Instrument, Hatfield, PA, USA) were used to control the gas composition inside the reactor. The furnace temperature was also controlled in order to set the temperature in the reactor. The outlet gas was connected to an infrared CO/CO₂ gas analyzer. The gas mixture was analyzed online with an infrared NGA 2000 gas analyser (Emerson Process Management, Hasselroth, Hesse, Germany). The gas concentrations were recorded each minute using the MLT Analyzer software (Version 3.6.X, Emerson Process Management, Hasselroth, Hesse, Germany), then it was possible to represent the evolution of CO and CO₂ concentrations with time. The yield of CO conversion was evaluated using Equation (2):

$$\text{CO conversion\%} = \left(\frac{[\text{CO}]_{\text{in}} - [\text{CO}]_{\text{out}}}{[\text{CO}]_{\text{in}}} \right) \times 100 \quad (2)$$

$[\text{CO}]_{\text{in}}$ is the CO inlet gas concentration.

$[\text{CO}]_{\text{out}}$ is the CO outlet gas concentration.

3. Results

3.1. Physico-Chemical Characterization

3.1.1. XRD

The diffractograms of the different catalysts, obtained by varying the RV/OV ratio and with a constant metal loading of 10 wt%, are shown in Figure 3. As shown in Figure 3a, all 10NiAl–*x* catalysts exhibited broad diffraction peaks of NiAl₂O₄ phase (JCPDS 01–078–6951) without any obvious diffraction peaks of NiO phase. These peaks, corresponding to NiAl₂O₄, can be also attributed to a defect spinel of $\gamma\text{-Al}_{2.67}\text{O}_4$ phase (JCPDS 04–005–4662), since the corresponding diffractogram overlaps those of nickel aluminates. No clear changes were observed in the peak positions, while a very slight variation in the peak intensities can be revealed when changing the RV/OV ratio. Compared to previous studies carried-out on 10 wt% Ni–Al₂O₃ catalyst, conflicting information can be found about the state of Ni. Formation of a defect NiAl₂O₄ phase has been reported by Li et al. [41] and Kiš et al. [42]. Other authors have shown that NiO and NiAl₂O₄ phases were the main present phases [43]. Differently, in other studies, only $\gamma\text{-Al}_2\text{O}_3$ and NiAl₂O₄ phases were formed, and NiO species displayed to be highly dispersed on $\gamma\text{-Al}_2\text{O}_3$ support by the formation of NiAl₂O₄ phase [44,45].

The XRD pattern of 10CoAl–*x* catalyst samples is shown at Figure 3b. All 10CoAl–*x* catalysts exhibited diffraction peaks of a defect spinel γ -alumina ($\gamma\text{-Al}_{2.67}\text{O}_4$) (JCPDS 04–005–4662), that coincided with the XRD spectra of stoichiometric CoAl₂O₄ spinel (JCPDS 00–003–0896). Then, it was not possible to show the formation of Co₃O₄, as its XRD spectra coincides with the diffraction peaks of $\gamma\text{-Al}_{2.67}\text{O}_4$ and CoAl₂O₄. Three explanations were possible: cobalt oxide was highly dispersed on the surface of $\gamma\text{-Al}_{2.67}\text{O}_4$, or a spinel phases was formed by solid reaction of cobalt oxide with $\gamma\text{-Al}_{2.67}\text{O}_4$ in the lattice, or cobalt oxide was not visible due to the detection threshold of XRD (to the small size of the oxide particles or to low concentration, below 1 wt%). A glancing view over the intensity of the signals reveals that the intensity of the diffraction peaks gradually increases by increasing the RV/OV value from 0.9 to 1.1. These peaks become sharper and more consistent for the 10CoAl–1.1 catalyst sample. The increase in intensity and sharpness of the peaks may be due to the higher amount of CoAl₂O₄ spinel in the catalyst. On the other hand, low amount of fuel (fuel lean conditions: R = 0.9) led to a significant decrease in crystallinity, indicating that $\gamma\text{-Al}_{2.67}\text{O}_4$ is the major phase in 10CoAl–0.9 catalyst. Formation of cobalt aluminates spinel structure seems to be more evident in the 10CoAl–1.1 sample, probably being the solid reaction between cobalt species and alumina facilitated at higher RV/OV ratio. Crystallinity enhancement could be attributed to the spinel formation, which might be

promoted by the higher flame temperature reached by increasing the RV/OV ratio [46] and improving the cations migration into the lattice. XRD results of 10CoAl- x catalyst samples are in agreement with previous studies. Indeed, formation of cobalt aluminates is quite a common phenomenon in cobalt oxide-alumina systems [47] regardless of their method of synthesis or cobalt metal loadings [48–50].

Figure 3c shows well-defined XRD patterns of 10CuAl- x catalyst samples. They all presented α -Al₂O₃ (JCPDS 00–042–1468 and CuO (JCPDS 00–005–0661) diffraction peaks. Contrary to the other samples, γ -Al_{2.67}O₄ or CuAl₂O₄ spinel phases are not detected for 10CuAl- x catalyst samples. Moreover, the 10CuAl-1.0 catalyst sample displayed high intensity diffraction peaks of α -Al₂O₃, as compared to those obtained in non-stoichiometric conditions, indicating that the 10CuAl-1.0 catalyst presents a higher crystallinity. The XRD patterns of 10CuAl- x were different from those obtained by Remuka [51] and Yao [52] who prepared CuO-Al₂O₃ catalysts with the impregnation method. The impregnation method leads to the formation of CuO species and CuAl₂O₄ phase.

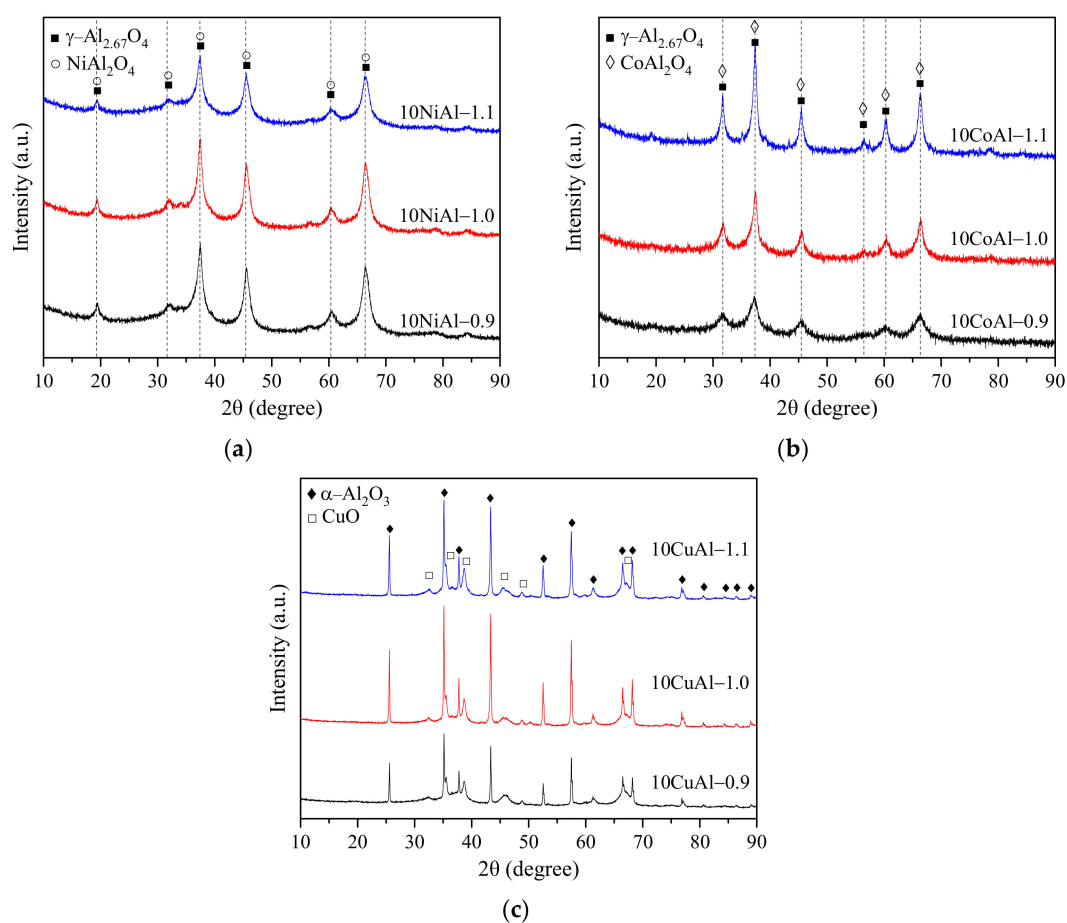


Figure 3. XRD patterns of (a) 10NiAl- x , (b) 10CoAl- x and (c) 10CuAl- x calcined sample.

A mixture of γ -alumina and metal aluminates (MAl₂O₄) were observed for 10NiAl- x and 10CoAl- x catalyst samples, while the presence of CuO and α -Al₂O₃ phases was found for the 10CuAl- x catalyst. These results suggest that the urea-nickel/cobalt nitrates mixtures lead to the formation of γ -alumina and the metal oxides (NiO or CoO) that further react to form MAl₂O₄ in a solid state reaction. The presence of CuO and α -Al₂O₃ separated phases in 10CuAl- x samples and the existence of γ -alumina in 10NiAl- x and 10CoAl- x samples treated at high temperatures raise questions about the nucleation and crystallization process of the different phases. Indeed, according to the literature [53–57], the formation of well-crystallized α -Al₂O₃ occurs at high temperatures above ≈ 1100 °C, while γ -Al₂O₃ is obtained at lower temperatures (<800 °C). On the other hand, it is generally acknowledged that the existence of aluminates spinel phases is detected at elevated temperatures

≈ 700 °C. Various theories are presented in the literature to explain the spinel formation, but it is very difficult to obtain an unambiguous knowledge on the formation process. During the combustion process the formation of Co, Ni, and Al oxide can reasonably take part. Nevertheless, at the high temperature reached during SC, solid state reactions can take part, and spinel phases can be formed starting from the individual oxides by counter-diffusion of cations in the solid, as already suggested in the '60 by Schmalzried [47]. The same author reported on the possibility of the cations and oxygen transfers also in the vapor phase. This mechanism was confirmed by Pettit et al. [58] that showed the growth of the spinel phase at the NiO-NiAl₂O₄ and NiAl₂O₄-Al₂O₃ interfaces. A different mechanism was reported by Nakano et al. [59] that observed the reaction of CoO and Al₂O₃ by inter-diffusion of Co and Al ions through a rigid oxygen lattice to form the spinel CoAl₂O₄. Thanks to the use of spark source mass spectrometry, the same group [58] was able to proposed the following mechanisms for spinel formation from AO and B₂O₃ type oxides: inter-diffusion of the two cations, parallel diffusion of A (or B) and oxygen ions, and the diffusion of electrons and A and B cations through the lattice in presence of transport of oxygen in the gas phase. It is not possible to state which mechanisms prevails during the formation of the binary catalyst synthesized in the present study, but the heterogeneity of the phase distribution enlightened by TEM/EDX analysis can be related to the presence of different reaction routes for the spinel formation. There were no changes in the phases present in the catalyst, and no detectable peaks of NiO or Co_xO_y species, when varying the RV/OV ratio. These observations suggest that the RV/OV ratio do not inhibit the spinel formation (at least in the studied RV/OV range). Depending of the RV/OV ratio, the quantity of oxygen atoms in the reaction medium can vary (being higher for the lowest RV/OV ratio), then the mechanism involving oxygen transport might prevail. At high RV/OV ratio, counter- or inter-diffusion of the cations are the most reasonable mechanisms for the formation of the spinel phase. On the other hand, the RV/OV ratio seems to affect the crystallinity degree of the obtained phases. Indeed, in most cases, fuel-lean and fuel-rich conditions result in a decrease of the XRD signal intensities, when compared to catalysts obtained under stoichiometric compositions (RV/OV = 1.0) and that exhibit an optimal crystallinity. A plausible explanation can be that the incomplete reaction between urea and metal nitrates leads to amorphous materials. Thus, the proper combination of chemical reagents is essential for optimizing the combustion reactions.

3.1.2. N₂ Adsorption-Desorption Isotherms

The textural properties of the calcined 10MAl-x catalyst samples were determined starting from the N₂ adsorption-desorption isotherms (Figure 4). Type I isotherms were observed for 10NiAl-x samples, which shows that these materials are microporous. The H4 hysteresis loops can be due to the presence of narrow slit-like pores (Figure 4a). Figure 4b corresponds to the isotherms of the CoAl-0.9 and CoAl-1.0 samples. The profiles correspond to type (I+IV) isotherms, characteristic of microporous and mesoporous solids, with H4 hysteresis loops. On the other hand, the 10CoAl-1.1 sample showed type II isotherm, corresponding to macroporous solids, with H3 hysteresis loop, associated to the formation of aggregates with slit-shaped pores. All 10CuAl-x catalysts isotherms correspond to type II isotherms with H3 hysteresis loops (Figure 4c).

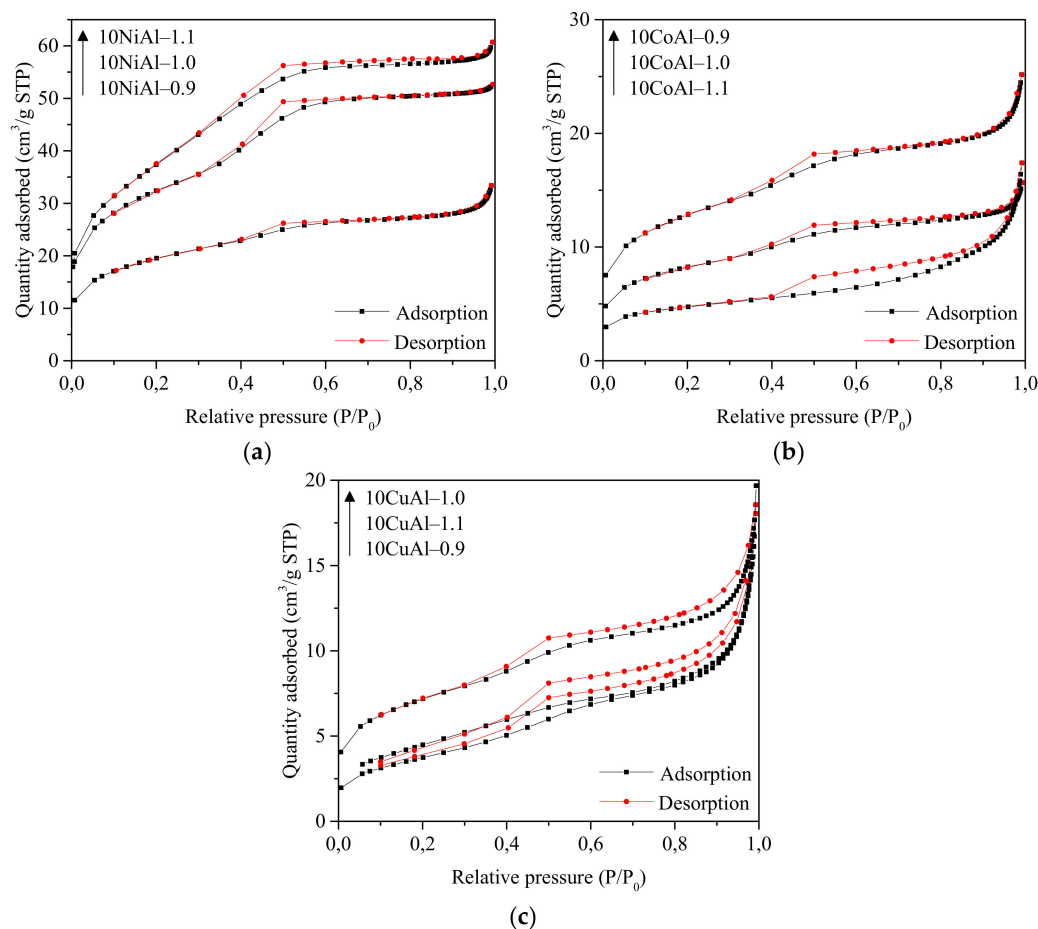


Figure 4. N_2 adsorption-desorption isotherm of (a) $10NiAl-x$, (b) $10CoAl-x$ and (c) $10CuAl-x$ calcined sample.

Table 2 lists the transition metal loadings (Ni, Co and Cu) (wt%), determined by XRF, and the textural properties of the $10MAI-x$ samples. The BET surface area of the $10NiAl-x$ calcined catalysts with different RV/OV varied from 69.4 to 135.1 m^2g^{-1} ; the $10NiAl-1.1$ catalyst exhibited the highest surface area. The pore volume was in the $0.04-0.08$ cm^3g^{-1} range, while the average pore diameter was centered between 2.7 and 3.5 nm. It seems that the pore volume and the surface area are correlated, while the decrease of pore volume induced larger average pore diameter. The increase of the RV/OV ratio from 0.9 to 1.1 led to higher surface areas. Moreover, the meso-structures of $10NiAl-x$ catalysts were sensitive to the RV/OV ratio. The pore volume increased and the pore diameter slightly decreased when the RV/OV value rises from 0.9 to 1.1 . Table 2 lists the transition metal loadings (Ni, Co and Cu) (wt%), determined by XRF, and the textural properties of the $10MAI-x$ samples. The BET surface area of the $10NiAl-x$ calcined catalysts with different RV/OV varied from 69.4 to 135.1 m^2g^{-1} ; the $10NiAl-1.1$ catalyst exhibited the highest surface area. The pore volume was in the $0.04-0.08$ cm^3g^{-1} range, while the average pore diameter was centered between 2.7 and 3.5 nm. It seems that the pore volume and the surface area are correlated, while the decrease of pore volume induced larger average pore diameter. The increase of the RV/OV ratio from 0.9 to 1.1 led to higher surface areas. Moreover, the meso-structures of $10NiAl-x$ catalysts were sensitive to the RV/OV ratio. The pore volume increased and the pore diameter slightly decreased when the RV/OV value rises from 0.9 to 1.1 .

Table 2. Elemental analysis and textural properties of the 10MAI–x calcined catalysts.

Sample	Metal Loading ¹ (wt%)	BET Surface Area (m ² g ⁻¹)	Pore Volume ² (cm ³ g ⁻¹)	Pore Diameter ³ (nm)
10NiAl–0.9	9.64	69.4	0.04	3.5
10NiAl–1.0	10	115.3	0.07	2.9
10NiAl–1.1	10.30	135.1	0.08	2.7
10CoAl–0.9	10.14	45.9	0.03	3.9
10CoAl–1.0	9.97	31.5	0.02	3.8
10CoAl–1.1	10.70	16.1	0.02	7.9
10CuAl–0.9	9.80	13.5	0.03	7.0
10CuAl–1.0	9.90	25.7	0.03	5.0
10CuAl–1.1	10.70	16.4	0.03	6.5

¹ XRF elemental analysis. ² BJH Desorption pore volume. ³ BJH Desorption average pore diameter.

The surface area of the 10CoAl–x catalysts varied from 16.1 to 45.9 m²g⁻¹ while the pore volume was between 0.02 and 0.03 cm³g⁻¹, and the average pore size ranged from 3.8 to 7.9 nm. The 10CoAl–0.9 catalyst presented the highest surface area as well as the highest average pore size. When compared to the 10NiAl–x catalyst, the RV/OV ratio seems to have an opposite effect on the textural properties of the 10CoAl–x catalyst. In fact, the surface area significantly decreased by increasing the fuel/nitrates ratio. Meanwhile, the pore diameter increased when the RV/OV value rose from 0.9 to 1.1. On one hand, this is probably due to the higher RV/OV ratio that can lead to a higher flame temperature, thus promoting the sintering and the particle agglomeration, resulting in a lower surface area of the final product. On the other hand, the cobalt aluminates formation may affect the textural properties of the materials and consequently decreases the surface area [30,60].

The 10CuAl–x calcined catalysts presented a lower BET surface area than the nickel or cobalt based catalysts. The 10CuAl–1.0 catalyst presented the largest surface area of 25.7 m²g⁻¹ and the smallest pore diameter, while the 10CuAl–0.9 catalyst exhibited the lowest surface area of 13.5 m²g⁻¹ and the largest pore size. The pore volume remained constant when varying the RV/OV ratio.

The solution combustion method tends to form materials with low surface area. Combustion may be at the origin of this limitation. The highest the combustion temperature is, the lowest the surface area will be, due to particle sintering and agglomeration. Among the different samples synthesized using various RV/OV ratios, 10NiAl–1.1 presented the highest surface area, while the 10CuAl–0.9 catalyst presented the smallest surface area. The RV/OV ratio has an important effect on the textural properties of the various catalysts. This could be explained by the fact that the combustion behavior of different urea/nitrates mixtures affects the exothermicity of the combustion reaction and the volume of the gases generated during the combustion process. Both effects contribute to the tuning of the final textural properties of the combustion-synthesized samples.

3.1.3. SEM

The SEM micrographs of the 10MAI–x samples, with various RV/OV ratios, are collected in Figure 5. The agglomerates of the 10NiAl–x samples presented plate-like morphology, with an average size of 50 μm. The surface of the agglomerated particles showed the presence of cracks and voids, which reflects the inherent nature of the combustion reaction. No significant differences were observed in the morphology of the different 10NiAl–x samples.

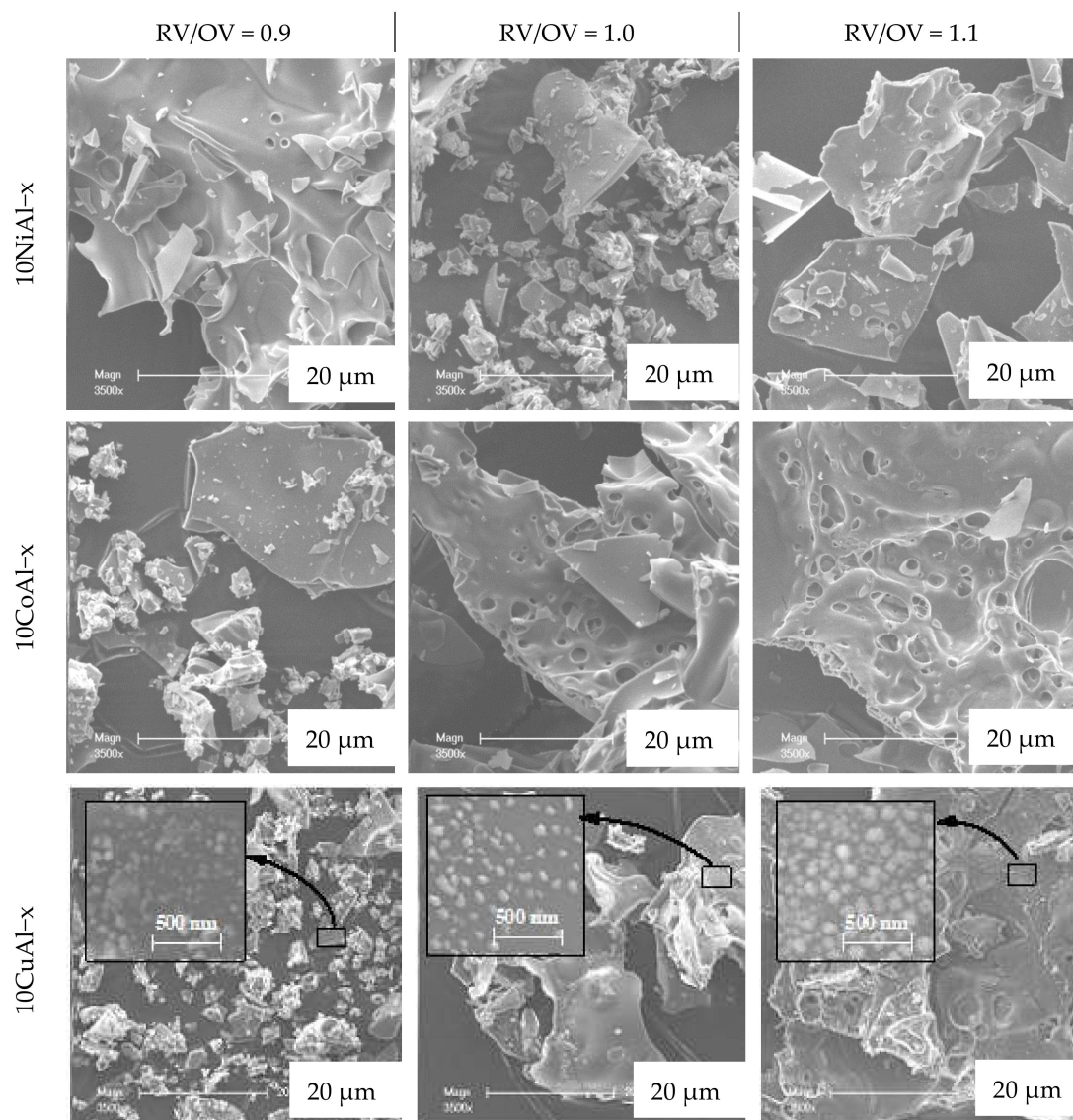


Figure 5. SEM images of the 10MAI-x calcined catalysts.

Some distinctions could be observed in the morphology of the different 10CoAl-x samples. For the sample 10CoAl-0.9, the SEM images exhibited “flaky-like” morphology, similar to that obtained for the 10NiAl-x samples. For the 10CoAl-1.0 and 10CoAl-1.1 samples, the micrographs presented foamy agglomerated particles with plate form and a higher average size than that of 10CoAl-0.9, and the presence of voids at the surface, originating from the combustion gases. The temperature and the amount of evolved gas increase with the RV/OV ratio, during the combustion process, resulting in the agglomerates growth and large holes [61,62].

The micrographs of 10CuAl-x samples showed foamy and “flaky-like” agglomerated particles. The SEM images with magnification of $\times 100,000$ show quasi-spherical nanoparticles, which could be attributed to the formation of copper oxide nanoparticles (also confirmed by EDX analysis—not shown). The size and distribution of copper oxide nanoparticles at the surface of the different samples are quite different. For the 10CuAl-0.9 catalyst, small particle size and regional agglomeration are observed. For the 10CuAl-1.0 catalyst, the nanoparticles are uniformly dispersed. A significantly larger particle size and apparent agglomeration are observed on the 10CuAl-1.1 catalyst. This result can be explained by the increase of combustion temperature with the RV/OV ratio, and then to the sintering of copper oxides particles.

The agglomerates of the combustion-synthesized 10MAI-x catalysts presented a foamy and “flaky-like” morphology. This morphology is commonly observed for combustion-synthesized alumina powders [24]. Therefore, the addition of transition metal oxides to alumina induces textural modifications without any substantial changes at the microscopic scale. The catalytic activity may be improved by the foamy morphology which facilitates the access of bulk active sites. The surface features of the calcined samples prepared at various RV/OV are somewhat different. The 10NiAl-x and 10CoAl-x samples presented non-defined surfaces, while 10CuAl-x samples presented quasi-spherical nanoparticles all over the surface. The agglomeration behavior and particle size of the observed nanoparticles were strongly affected by the RV/OV ratio. The lower the RV/OV ratio, the smaller the particles formed. The increase of the RV/OV ratio resulted in a greater agglomeration and highly foamed materials. These results suggested that a higher RV/OV ratio produces a higher combustion temperature and larger volume of gaseous products. There were no clear changes in the morphology of nickel and cobalt based catalysts, while a severe agglomeration with irregular distribution of agglomerated particles were detected on the copper-based catalysts. Probably an uncontrolled combustion reaction takes place by further increasing or decreasing the RV/OV ratio. Thus, it can be roughly concluded that the control of the phase formation and of the morphologies of the products is strictly linked to the stoichiometry of the reactants.

3.1.4. XPS

The Ni 2p_{3/2}, Co 2p_{3/2} and Cu 2p_{3/2} XP spectra of 10MAI-x calcined samples are presented in Figure 6. For facilitating the comparison, the electron binding energies (BE) of 10MAI-x catalyst samples are listed in Table 3. The surface of 10NiAl-x catalysts showed a main peak corresponding to Ni 2p_{3/2} located at 855.9 eV, and two satellites corresponding to Ni²⁺ in the NiAl₂O₄ spinel respectively at 861.9 ± 0.2 eV and 866.8 ± 0.4 eV, as described in the literature. The presence of Ni(OH)₂ in 10NiAl-x catalysts has been excluded due to the absence of a peak close to 861 eV, corresponding to the asymmetry of the peak located at 855.9 eV [63–66]. In order to quantitatively compare the Ni concentration on the surface of the different catalysts, the surface Ni/Al atomic ratios were calculated by XPS. As shown in Figure 6a, the measured Ni/Al atomic ratios slightly vary from 0.074 to 0.086. A higher surface Ni/Al atomic ratio was observed for the 10NiAl-1.0 sample, indicating a higher Ni concentration on the surface of the 10NiAl-1.0 catalyst.

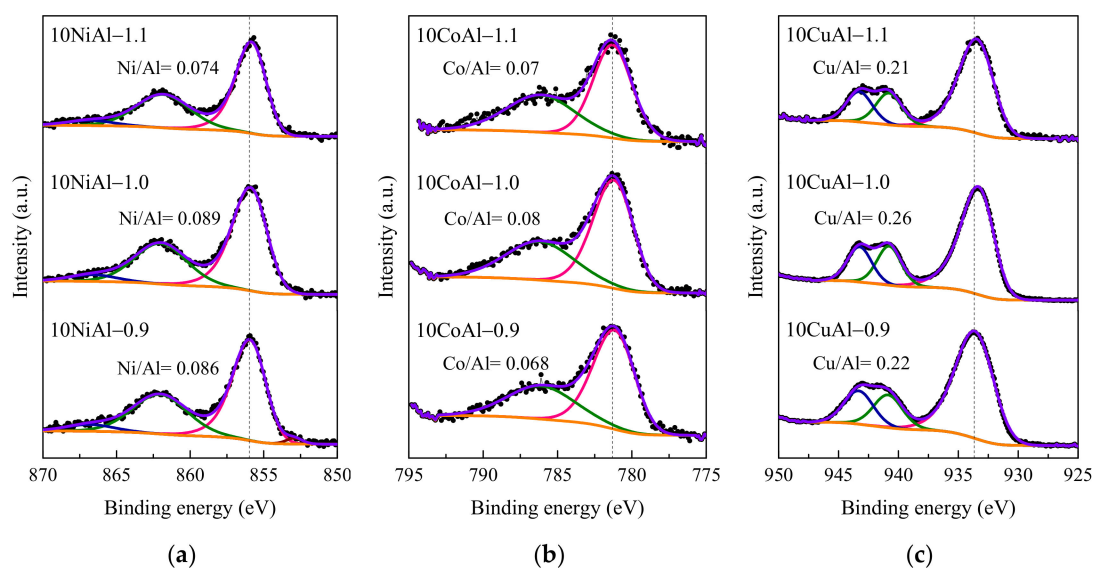


Figure 6. (a) Ni 2p_{3/2}, (b) Co 2p_{3/2} and (c) Cu 2p_{3/2} XP spectra for 10MAI-x calcined samples.

Table 3. BEs of the Ni 2p_{3/2}, Co 2p_{3/2}, and Cu 2p_{3/2} XP spectra for 10MAl–x calcined samples.

RV/OV Ratio	Ni 2p _{3/2} (eV)	Co 2p _{3/2} (eV)	Cu 2p _{3/2} (eV)
0.9	856.02	781.31	933.68
1.0	855.94	781.33	933.36
1.1	855.86	781.42	933.58

The Co 2p_{3/2} spectra, acquired for the 10CoAl–x catalysts, showed peaks at approximately 781.31–781.42 eV with their broad satellite peaks at around 786.21, 786.32 and 786.22 eV. These peaks can be assigned to Co²⁺ in CoAl₂O₄, based on values reported in the literature [67,68]. They suggest that CoAl₂O₄ is the predominant phase present on the catalyst surfaces. Co₂O₃, CoO and Co₃O₄ phases were not detected (absence of peak at 780 eV related to these oxides) [63], as well as Co(OH)₂ phase (no peak at 780.4 eV) [63]. The values of the relative ratio of Co species determined by XPS are included in Figure 6b. Also, for the Co-containing samples, the values of Co/Al ratios were almost constant, slightly varying from 0.068 to 0.08.

The Cu 2p_{3/2} signals obtained for the 10CuAl–x catalysts could be assigned to a principal peak located at 933.36–933.68 eV and two satellites at BE of 940.88 ± 0.1 and 943.1 ± 0.2 eV, corresponding to Cu²⁺ in CuO, by referring to literature values [69,70]. CuAlO₂ and Cu₂O phases were not detected at the surface of the different 10CuAl–x catalysts (no peak at 932 eV and 932.4 eV) [70–73]. Likewise, there was no peak at 935 eV, which indicates that Cu(OH)₂ and CuAl₂O₄ phases are also absent on the surface of these catalysts [68,69,71]. The values of the Cu/Al surface ratios calculated from XPS analysis are included in Figure 6c. The maximum Cu/Al atomic ratio of 0.26 was achieved in the 10CuAl–1.0 catalyst obtained from stoichiometric conditions, suggesting a higher presence of Cu species over the alumina surface.

According to the XPS survey, nickel and cobalt oxides were present on the surface of the 10NiAl–x and 10CoAl–x catalysts as metal aluminates surface spinels (MAl₂O₄), while free copper oxides were the main phases observed at the surface of 10CuAl–x catalysts. This suggests that γ–alumina might easily react in the solid phase with Ni- and Co- metal oxides than α–alumina with Cu-oxide. XPS also offered interesting information about the dispersion and the proportion of the catalytic species of these catalysts. Surprisingly, the surface M/Al atomic ratios were maximized for the samples obtained in stoichiometric conditions (RV/OV = 1). For the 10NiAl–x and 10CoAl–x catalysts, a lower surface M/Al atomic ratio was obtained for the 10MAl–1.1 sample. The surface M/Al ratio is expected to affect, subsequently, the catalytic activity of the combustion synthesized catalysts.

3.2. Catalyst Activity

3.2.1. Evaluation of the Catalyst Performances through CO Oxidation

The conversion of CO on Ni, Cu and Co-containing catalysts is presented in Figure S1 (a–1,a–2,a–3) (Supplementary Materials File) for a wide range of temperature from ambient up to 500 °C. The performances of the different catalysts were estimated in steady state conditions for 30 min at specific temperatures, defined according to the specific activity of the catalysts (between 100 and 500 °C).

Results are presented in Figure 7a–c. Table 4 summarizes the different values of the characteristic temperatures corresponding to the light-off (1% of CO conversion into CO₂), half and total oxidation of CO. During the transient experiments, the oxidation of CO over the 10NiAl–0.9, 10NiAl–1.0 and 10NiAl–1.1 catalysts began respectively at 270, 254, and 301 °C. The CO conversion on overall 10NiAl–x catalysts gradually increased, by increasing the temperature, without reaching the total conversion of CO at 500 °C. The oxidation of CO observed at 500 °C with the 10NiAl–0.9, 10NiAl–1.0 and 10NiAl–1.1 catalysts was of 29%, 44% and 19%, respectively. In the 10NiAl–x series, the best activity was obtained for the 10NiAl–1.0 catalyst, and the worst for 10NiAl–1.1. Thus, the enhancement of the RV/OV ratio did not show any benefit for the oxidation of CO on the nickel-based catalysts. As shown in Figure 7a, the 10NiAl–x catalysts presented low CO oxidation performances (less than 5% of conversion into

CO₂) at 300 °C, for the experiments performed in steady state conditions. Then, the conversion of CO into CO₂ reached 7%, 9% and 5% at 400 °C, for the 10NiAl-0.9, 10NiAl-1.0 and 10NiAl-1.1 catalyst, respectively. The 10NiAl-x catalysts presented a relatively low activity in the 300-500 °C range, but the CO conversion was enhanced when increasing the temperature.

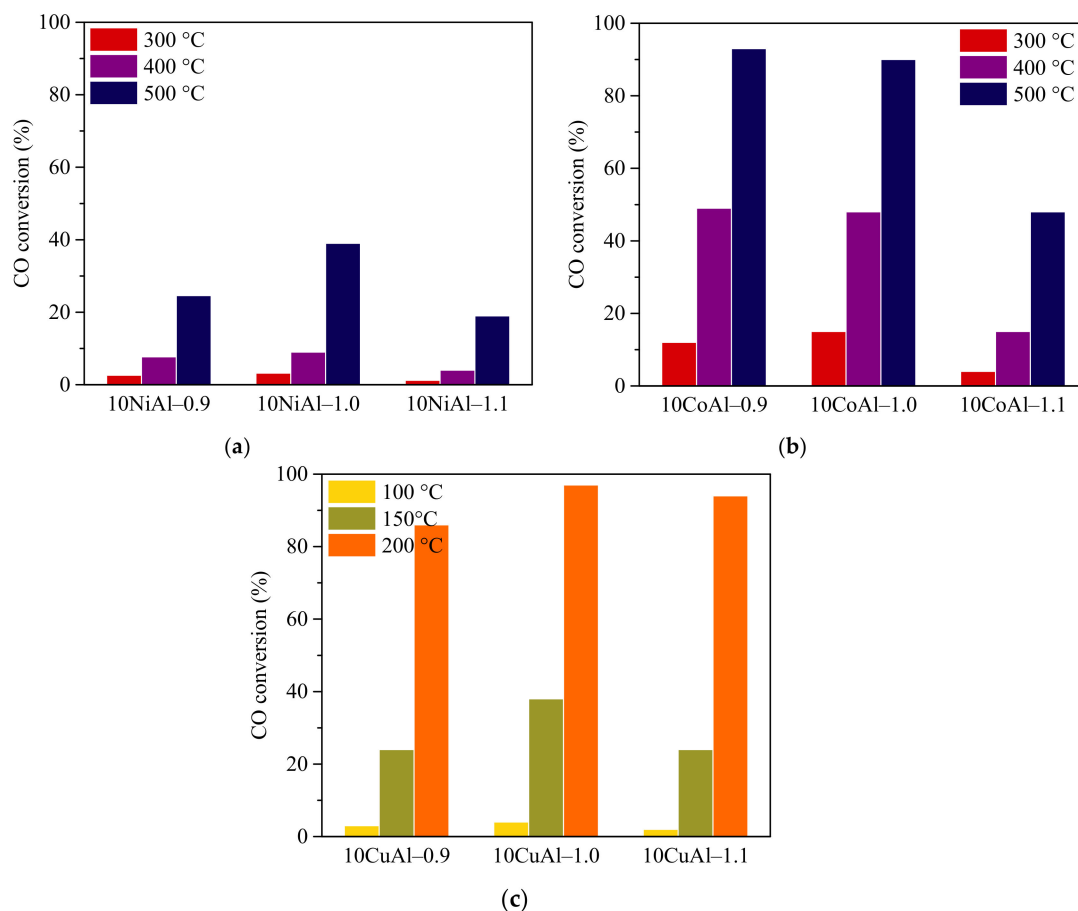


Figure 7. (a, b, c) CO conversion under steady state conditions over the 10MAI-x calcined catalysts.

Table 4. Effect of RV/OV ratio on the light-off, T₅₀ and T₁₀₀ temperatures of the 10MAI-x catalyst samples.

Sample	T ₁	T ₅₀	T ₁₀₀
10NiAl-0.9	270	–	–
10NiAl-1.0	254	–	–
10NiAl-1.1	301	–	–
10CoAl-0.9	209	412	–
10CoAl-1.0	235	406	–
10CoAl-1.1	246	497	–
10CuAl-0.9	96	190	250
10CuAl-1.0	90	170	225
10CuAl-1.1	97	180	250

The catalytic activity of the 10CoAl-0.9 and 10CoAl-1.0 catalysts in CO oxidation was higher than that of the 10CoAl-1.1 catalyst. The oxidation of CO over the 10CoAl-0.9 and 10CoAl-1.0 catalysts started respectively at 209 °C and 235 °C, while on the 10CoAl-1.1 catalyst, the CO conversion started only at 246 °C (Figure S1 a–2). The CO conversion gradually increased to reach 50% at around 400 °C over the 10CoAl-0.9 and 10CoAl-1.0 catalysts. For the 10CoAl-1.1 catalyst the half CO conversion

was not yet achieved at 400 °C. The optimal CO conversion obtained at 500 °C for 10CoAl–0.9 and 10CoAl–1.0 catalysts was of 90%, while the 10CoAl–1.1 catalyst showed the lowest final conversion (approximately 50%). According to Figure 7b, the 10CoAl–0.9 and 10CoAl–1.0 catalysts presented comparable activities, with a CO conversion of approximately 50% and 90% at 400 and 500 °C, respectively. Whereas, the 10CoAl–1.1 catalyst had significantly lower activity than the 10CoAl–0.9 and 10CoAl–1.0 catalysts and the CO conversion was of 15% and 50% at 400 and 500 °C, respectively. It is worth pointing out that, similarly to nickel based catalysts prepared at RV/OV ratio higher than 1, the catalytic activity of cobalt based catalysts for the oxidation of CO is lowered.

The performances of the 10CuAl–*x* catalysts for the oxidation of CO were characterized by a relatively high conversion at low temperatures (less than 100 °C). The CO conversion sharply increased, by increasing the temperature, to reach the maximum between 190 and 250 °C. The catalytic activities of copper-based catalysts were fairly better than cobalt and nickel-based catalysts for the oxidation of CO. The presence of CuO and bulk CuO species at the surface of these catalysts is probably at the origin of the high conversion rate of CO in the presence of oxygen (Figure 7c). The 10CuAl–1.0 catalyst exhibited the highest CO conversion rates with values around 5%, 40% and 98% at 100 °C, 150 °C and 200 °C, respectively (Figure 7). The 10CuAl–0.9 catalyst displayed the lowest CO conversion rates with 25% and 85% at 150 °C and 200 °C, respectively.

The catalytic results show that the performance of the different samples towards CO oxidation was strongly affected by the reaction temperature. This classical behavior it is probably not only due to the increasing reaction kinetics. In this case, the reaction temperature affects the interaction of the adsorbed molecules (CO and O₂) on the metal oxide surfaces (O₂ adsorption is inhibited by CO at low temperature). Then, at higher temperature, part of the CO desorbs from the catalytic sites that free are able to adsorb the O₂; CO and O₂ can then react on the catalyst surface to produce CO₂. It is seen that, by increasing the RV/OV ratio from 0.9 to 1.1 for 10NiAl–*x* and 10CoAl–*x* catalyst samples, more aluminate spinel structures are formed and lower CO conversion are observed. Among the different synthesized catalysts, the 10NiAl–*x* series exhibited the largest surface areas and the worst performances for converting CO, whereas the 10CuAl–*x* catalyst samples had the smallest surface areas and the highest activities. In addition, it was found that stoichiometric compositions (RV/OV = 1.0) lead to an optimal crystallinity and that CO oxidation is optimal for the catalysts presenting a RV/OV ratio of 1.0. The present results suggest that CO oxidation reaction is structure sensitive and that the alumina-metal interaction plays a crucial role on the CO oxidation activity. On the basis of the activity results, it seems that the catalyst activity derives primarily from the extent of the interaction between the metal oxide and alumina. The interaction of metal oxide with alumina affects the bulk and surface chemical composition, structural properties, and active sites dispersion which further affect the catalytic performances. Meanwhile, the presence of free bulk metal oxide is mandatory for the CO oxidation activity.

3.2.2. Comparison of the Catalyst Performances with Similar Materials obtained with Different Methods

Many studies have been carried out on supported copper oxide catalysts. Most of these oxide catalysts were made by traditional synthesis methods. Pierron et al. [74] and Luo et al. [75] obtained a CO conversion of 50% at around 270 °C (reaction conditions: 4.8 vol% CO in air) and 250 °C (reaction conditions: 2.4 vol% CO and 1.2 vol% O₂ in N₂), using 10 wt% Cu–Al₂O₃ catalysts prepared by wet impregnation. Renuka et al. [76] used wet impregnation method to prepare 11 wt% Cu supported mesoporous alumina catalyst. Their results showed that the conversion of CO reached 100% at around 300 °C. The presence of reduced cationic species of Cu and metallic copper atoms induces a beneficial effect on CO oxidation. Severino et al. [77] reported a study of the effect of copper concentration (2–30 wt%) on the CO oxidation activity at 400 °C for 3h (reaction conditions: 5 vol% CO in air), using impregnation method. They showed that the activity of the catalysts increases by increasing the metal loading from 2 to 10 wt% (with a maximum CO conversion of about 85%), but the activity decreases

at higher concentrations (>10 wt%). Alumina-supported copper catalyst, prepared by impregnation method, was also studied by Jiang et al. [78]; 12 wt% CuO/Al₂O₃ catalyst showed a CO conversion (reaction conditions: 4 vol% CO, 17 vol% O₂ and 79% N₂) of 50% and 99% at around 200 °C and 260 °C, respectively [78].

Thormahlen et al. [79,80] reported a high catalytic activity of CoO_x/Al₂O₃ system using impregnation method and different oxidizing and reducing pretreatments prior to reaction. Pre-reduced cobalt oxide/alumina catalyst with 20 wt% CoO_x showed a CO conversion of 50% at 157 °C (reaction conditions: 1 vol% CO and 0.6 vol% O₂ in N₂) [80]. Later, Jansson et al. [81] clearly demonstrated the high activity of the pretreated CoO_x/Al₂O₃ system for CO oxidation. They reported a T₅₀ of 150 °C for pre-reduced CoO_x/Al₂O₃ catalyst compared to 80 °C for the pre-oxidized catalyst. Full conversion is reached at about 265 °C for the pre-reduced catalyst (reaction conditions: 2 vol% CO and 1.17 vol% O₂ in N₂). Wang et al. [82] prepared supported cobalt catalyst on Al₂O₃ (5 wt% as metal Co loading) by incipient wetness impregnation. A full conversion of CO was obtained at 300 °C (reaction conditions: 10 vol% O₂ and 4 vol% CO in He).

In comparison to copper and cobalt based catalysts, few references can be found, dealing with the activity of nickel-based catalysts for the CO oxidation reaction. This is essentially due to its low activity in CO oxidation. Nickel-based catalysts were studied by El-Shobaky et al. [83–85] and Chen et al. [86]. The study of El-Shobaky et al. was mainly focused on the physicochemical properties of NiO-Al₂O₃ systems, prepared by co-precipitation and impregnation. In their studies [83,84] they did not observe the formation of the spinel phase at temperatures below 850 °C. Higher activation temperatures (above 850 °C) resulted in the formation of the nickel aluminate phase. Chen et al. [86] clearly demonstrated the low activity of nickel-based catalysts for CO oxidation. Indeed, reduced 15 wt% Ni/Al₂O₃ catalyst showed full conversion of CO at around 500 °C.

4. Conclusions

In this study, variation of the reactant stoichiometry (RV/OV ratio) has demonstrated to be a well-settled approach for controlling the properties of the combustion-synthesized mixed oxides catalysts. Indeed, the stoichiometry and the nature of the metal in the nitrate precursor have an important impact for the control of the phase composition, surface area, micro/nanostructure characteristics, and surface chemical composition (surface M/Al atomic ratio). Based on the different characterizations, the control of the RV/OV ratio allows improving the properties of the catalysts prepared through the microwave-assisted SC method.

The performances of the different catalysts were correlated to their characterizations. Indeed, the catalysts prepared under stoichiometric composition (RO/RV = 1) presented the optimal structural properties and the best catalytic activities. At the opposite, the synthesis of catalysts with a non-stoichiometric RV/OV ratio led to a non-controlled combustion reaction, thus resulting to poor structural properties and lower CO oxidation activities.

Supplementary Materials: The following are available online at <http://www.mdpi.com/1996-1073/13/12/3126/s1>. Figure S1: (a-1, a-2, a-3) CO conversion under transient conditions over the 10MA-x calcined catalysts.

Author Contributions: Conceptualization, L.L. and J.B.; Investigation, K.F. and S.B.; Methodology, L.L.; Project administration, L.L. and S.B.; Resources, L.L. and S.B.; Supervision, L.L., J.B., K.C. and S.B.; Validation, S.B.; Visualization, K.F.; Writing—original draft, K.F.; Writing—review & editing, L.L. and S.B. All authors have read and agreed to the published version of the manuscript.

Funding: This research was funded by the Ministry of Higher Education and Research, Tunisia, Grant Number [2017-BALT-1037].

Acknowledgments: All physicochemical characterizations were done at IS2M. The authors would like to thank S. Hajjar (XPS), L. Michelin (XRF and XRD), L. Josien (SEM), H. Nouali (N₂-adsorption) for their contributions.

Conflicts of Interest: The authors declare no conflict of interest.

References

1. Védérine, J.C.; Fehete, I. Heterogeneous partial oxidation catalysis on metal oxides. *Comptes. Rendus. Chim.* **2016**, *19*, 1203–1225. [[CrossRef](#)]
2. Védérine, J.C. Metal Oxides in Heterogeneous Oxidation Catalysis: State of the Art and Challenges for a More Sustainable World. *Chem. Sus. Chem.* **2019**, *12*, 577–588. [[CrossRef](#)]
3. Twigg, M.V. Rôles of catalytic oxidation in control of vehicle exhaust emissions. *Catal. Today* **2006**, *117*, 407–418. [[CrossRef](#)]
4. Reddy, B.M. Redox properties of metal oxides. In *Metal Oxides: Chemistry and Applications*; CRC Press: New York, NY, USA, 2005.
5. Bion, N.; Can, F.; Courtois, X.; Duprez, D. Transition metal oxides for combustion and depollution processes. In *Metal Oxides in Heterogeneous Catalysis*; Elsevier: Amsterdam, The Netherlands, 2018; pp. 287–353, ISBN 9780128116319.
6. Kung, H.H. *Transition Metal Oxides: Surface Chemistry and Catalysis*, 1st ed.; Elsevier: Amsterdam, The Netherlands, 1989; ISBN 0444873945.
7. Anthony, P. *Transition Metal Oxides. An Introduction to Their Electronic Structure and Properties*, 1st ed.; Oxford University Press: Oxford, UK, 1992; ISBN 0198555709.
8. Kamal, M.S.; Razzak, S.A.; Hossain, M.M. Catalytic oxidation of volatile organic compounds (VOCs)—A review. *Atmos. Environ.* **2016**, *140*, 117–134. [[CrossRef](#)]
9. Royer, S.; Duprez, D. Catalytic oxidation of carbon monoxide over transition metal oxides. *Chem. Cat. Chem.* **2011**, *3*, 24–65. [[CrossRef](#)]
10. Schwarz, J.A.; Contescu, C.; Contescu, A. Methods for preparation of catalytic materials. *Chem. Rev.* **1995**, *95*, 477–510. [[CrossRef](#)]
11. Campanati, M.; Fornasari, G.; Vaccari, A. Fundamentals in the preparation of heterogeneous catalysts. *Catal. Today* **2003**, *77*, 299–314. [[CrossRef](#)]
12. Rao, C.N.R.; Biswas, K. *Essentials of Inorganic Materials Synthesis*, 1st ed.; John Wiley & Sons: Hoboken, NJ, USA, 2015; ISBN 9781118832547.
13. Lee, D.W.; Yoo, B.R. Advanced metal oxide (supported) catalysts: Synthesis and applications. *J. Ind. Eng. Chem.* **2014**, *20*. [[CrossRef](#)]
14. Carrier, X.; Royer, S.; Marceau, E. Synthesis of metal oxide catalysts. In *Metal Oxides in Heterogeneous Catalysis*; Elsevier: Amsterdam, The Netherlands, 2018; pp. 43–103, ISBN 9780128116319.
15. Schütz, M.B.; Xiao, L.; Lehnen, T.; Fischer, T.; Mathur, S. Microwave-assisted synthesis of nanocrystalline binary and ternary metal oxides. *Int. Mater. Rev.* **2017**, *63*, 341–374. [[CrossRef](#)]
16. Gawande, M.B.; Shelke, S.N.; Zboril, R.; Varma, R.S. Microwave-assisted chemistry: Synthetic applications for rapid assembly of nanomaterials and organics. *Acc. Chem. Res.* **2014**, *47*, 1338–1348. [[CrossRef](#)]
17. Bilecka, I.; Niederberger, M. Microwave chemistry for inorganic nanomaterials synthesis. *Nanoscale* **2010**, *2*, 1358–1374. [[CrossRef](#)]
18. Bhattacharya, M.; Basak, T. A review on the susceptor assisted microwave processing of materials. *Energy* **2016**, *97*, 306–338. [[CrossRef](#)]
19. Singh, S.; Gupta, D.; Jain, V.; Sharma, A.K. Microwave processing of materials and applications in manufacturing industries: A Review. *Mater. Manuf. Process.* **2015**, *30*, 1–29. [[CrossRef](#)]
20. Thostenson, E.T.; Chou, T.W. Microwave processing: Fundamentals and applications. *Compos. Part A Appl. Sci. Manuf.* **1999**, *30*, 1055–1071. [[CrossRef](#)]
21. Mingos, D.M.P. The applications of microwaves in chemical syntheses. *Res. Chem. Intermed.* **1994**, *20*, 85–91. [[CrossRef](#)]
22. Rosa, R.; Ponzoni, C.; Leonelli, C. Direct energy supply to the reaction mixture during microwave-assisted hydrothermal and combustion synthesis of inorganic materials. *Inorganics* **2014**, *2*, 191–210. [[CrossRef](#)]
23. Rosa, R.; Veronesi, P.; Leonelli, C. A review on combustion synthesis intensification by means of microwave energy. *Chem. Eng. Process. Process Intensif.* **2013**. [[CrossRef](#)]
24. Varma, A.; Mukasyan, A.S.; Rogachev, A.S.; Manukyan, K.V. Solution combustion synthesis of nanoscale materials. *Chem. Rev.* **2016**, *116*, 14493–14586. [[CrossRef](#)]
25. Moore, J.J.; Feng, H.J. Combustion synthesis of advanced materials: Part I. Reaction parameters. *Prog. Mater. Sci.* **1995**, *39*, 243–273. [[CrossRef](#)]

26. Wolf, E.E.; Kumar, A.; Mukasyan, A.S. Combustion synthesis: A novel method of catalyst preparation. *Catalysis* **2019**, *31*, 297–346. [[CrossRef](#)]
27. Aruna, S.T.; Mukasyan, A.S. Combustion synthesis and nanomaterials. *Curr. Opin. Solid State Mater. Sci.* **2008**, *12*, 44–50. [[CrossRef](#)]
28. Patil, K.C.; Aruna, S.T.; Mimani, T. Combustion synthesis: An update. *Curr. Opin. Solid State Mater. Sci.* **2002**, *6*, 507–512. [[CrossRef](#)]
29. González-Cortés, S.L.; Imbert, F.E. Fundamentals, properties and applications of solid catalysts prepared by solution combustion synthesis (SCS). *Appl. Catal. A Gen.* **2013**, *452*, 117–131. [[CrossRef](#)]
30. Patil, K.C.; Hegde, M.S.; Rattan, T.; Aruna, S.T. *Chemistry of Nanocrystalline Oxide Materials*; World Scientific Publishing: Singapore, 2008; ISBN 9789812793140.
31. Chen, C.C.; Huang, K.T. Parametric effects of low-temperature combustion synthesis of alumina. *J. Mater. Res.* **2005**, *20*, 424–431. [[CrossRef](#)]
32. Ozuna, O.; Hirata, G.A.; McKittrick, J. Pressure influenced combustion synthesis of γ - and α -Al₂O₃ nanocrystalline powders. *J. Phys. Condens. Matter.* **2004**, *16*, 2585–2591. [[CrossRef](#)]
33. Zhuravlev, V.D.; Bamburov, V.G.; Beketov, A.R.; Perelyaeva, L.A.; Baklanova, I.V.; Sivtsova, O.V.; Vasil'ev, V.G.; Vladimirova, E.V.; Shevchenko, V.G.; Grigorov, I.G. Solution combustion synthesis of α -Al₂O₃ using urea. *Ceram. Int.* **2013**, *39*, 1379–1384. [[CrossRef](#)]
34. Meng, F.; Tian, Z.; Zhang, F.; Tian, C.; Huang, W. Combustion synthesis of nanocrystalline Al₂O₃ powders using urea as fuel: Influence of different combustion aids. *Key Eng. Mater.* **2010**, *434–435*, 868–871. [[CrossRef](#)]
35. De Freitas, N.L.; Fagury-Neto, E.; Lira, H.L.; Gama, L.; Kiminami, R.H.G.A.; de Melo Costa, A.C.F. Combustion Synthesis of α -Al₂O₃ Powders. *Mater. Sci. Forum* **2006**, *530–531*, 631–636. [[CrossRef](#)]
36. Bhaduri, S.; Zhou, E.; Bhaduri, S.B. Auto Ignition Processing of Nanocrystalline α -Al₂O₃. *Nanostruct. Mater.* **1996**, *7*, 487–496. [[CrossRef](#)]
37. Huang, J.; Zhuang, H.; Li, W. Synthesis and characterization of nano crystalline BaFe₂O₁₉. *Mat. Res. Bull.* **2003**, *38*, 149–159.
38. Zhu, Y.J.; Chen, F. Microwave-assisted preparation of inorganic nanostructures in liquid phase. *Chem. Rev.* **2014**, *114*, 6462–6555. [[CrossRef](#)]
39. Jain, S.R.; Adiga, K.C.; Pai Verneker, V.R. A new approach to thermochemical calculations of condensed fuel-oxidizer mixtures. *Combust. Flame* **1981**, *40*, 71–79. [[CrossRef](#)]
40. Frikha, K.; Limousy, L.; Bouaziz, J.; Chaari, K.; Josien, L.; Nouali, H.; Michelin, L.; Vidal, L.; Hajjar-Garreau, S.; Bennici, S. Binary oxides prepared by microwave-assisted solution combustion: Synthesis, characterization and catalytic activity. *Materials* **2019**, *16*. [[CrossRef](#)]
41. Li, G.; Hu, L.; Hill, J.M. Comparison of reducibility and stability of alumina-supported Ni catalysts prepared by impregnation and co-precipitation. *Appl. Catal. A Gen.* **2006**, *301*, 16–24. [[CrossRef](#)]
42. Kiš, E.; Marinković-Nedučin, R.; Lomić, G.; Bošković, G.; Obadović, D.Ž.; Kiurski, J.; Putanov, P. Structural and textural properties of the NiO-Al₂O₃ catalyst. *Polyhedron* **1998**, *17*, 27–34. [[CrossRef](#)]
43. Zhao, A.; Ying, W.; Zhang, H.; Ma, H.; Fang, D. Ni-Al₂O₃ catalysts prepared by solution combustion method for syngas methanation. *Catal. Commun.* **2012**, *17*, 34–38. [[CrossRef](#)]
44. Zangouei, M.; Moghaddam, A.Z.; Arasteh, M. The influence of nickel loading on reducibility of NiO/Al₂O₃ catalysts synthesized by sol-gel method. *Chem. Eng. Res. Bull.* **2010**, *14*, 97–102. [[CrossRef](#)]
45. Ewbank, J.L.; Kovarik, L.; Diallo, F.Z.; Sievers, C. Effect of metal-support interactions in Ni/Al₂O₃ catalysts with low metal loading for methane dry reforming. *Appl. Catal. A Gen.* **2015**, *494*, 57–67. [[CrossRef](#)]
46. Gao, Y.; Meng, F.; Li, X.; Wen, J.Z.; Li, Z. Factors controlling nanosized Ni-Al₂O₃ catalysts synthesized by solution combustion for slurry-phase CO methanation: The ratio of reducing valences to oxidizing valences in redox systems. *Catal. Sci. Technol.* **2016**, *6*, 7800–7811. [[CrossRef](#)]
47. Schmalzried, H.; Pelton, A.D. Solid-State Reactions. *Angew. Chem. Intern.* **1963**, *2*, 251–254. [[CrossRef](#)]
48. Richardson, J.T.; Vernon, L.W. The magnetic properties of the cobalt oxides and the system cobalt-alumina. *J. Phys. Chem.* **1958**, *62*, 1153–1158.
49. Wang, W.J.; Chen, Y.W. Influence of metal loading on the reducibility and hydrogenation activity of cobalt/alumina catalysts. *Appl. Catal.* **1991**, *77*, 223–233. [[CrossRef](#)]
50. Chin, R.L.; Hercules, D.M. Surface spectroscopic characterization of cobalt-alumina catalysts. *J. Phys. Chem.* **1982**, *86*, 360–367. [[CrossRef](#)]

51. Renuka, N.K.; Shijina, A.V.; Praveen, A.K.; Aniz, C.U. Redox properties and catalytic activity of CuO/ γ -Al₂O₃ meso phase. *J. Colloid Interface Sci.* **2014**, *434*, 195–200. [[CrossRef](#)]
52. Yu Yao, Y.F.; Kummer, J.T. A study of high temperature treated supported metal oxide catalysts. *J. Catal.* **1977**, *46*, 388–401. [[CrossRef](#)]
53. Zhou, R.S.; Snyder, R.L. Structures and transformation mechanisms of the η , γ and θ transition aluminas. *Acta Crystallogr. Sect. B Struct. Sci.* **1991**, *47*, 617–630. [[CrossRef](#)]
54. Levin, I.; Brandon, D. Metastable alumina polymorphs: Crystal structures and transition sequences. *J. Am. Ceram. Soc.* **2005**, *81*, 1995–2012. [[CrossRef](#)]
55. Dynys, F.W.; Halloran, J.W. Alpha alumina formation in alum-derived gamma alumina. *J. Am. Ceram. Soc.* **1982**, *65*, 442–448. [[CrossRef](#)]
56. Takashi, S.; Hideo, W.; Fuji, M.; Minoru, T. Structural properties and surface characteristics on aluminum oxide powders. *Annu. Rep. Res. Cent. Ceram. Eng.* **2009**, *9*, 23–31. [[CrossRef](#)]
57. Trueba, M.; Trasatti, S.P. γ -Alumina as a support for catalysts: A review of fundamental aspects. *Eur. J. Inorg. Chem.* **2005**, 3393–3403. [[CrossRef](#)]
58. Pettit, F.S.; Randklev, E.H.; Felten, E.J. Formation of NiAl₂O₄ by Solid State Reaction. *J. Am. Ceram. Soc.* **1966**, *49*, 199–203.
59. Nakano, M.; Yamaguchi, G.; Saito, K. Role of Oxygen in Spinel Formation from MgO and Al₂O₃. *J. Ceram. Assoc. Japan* **1971**, *79*, 92–96. [[CrossRef](#)]
60. Avgouropoulos, G.; Ioannides, T. Selective CO oxidation over CuO-CeO₂ catalysts prepared via the urea-nitrate combustion method. *Appl. Catal. A Gen.* **2003**, *244*, 155–167. [[CrossRef](#)]
61. Naveen, C.S.; Dinesha, M.L.; Jayanna, H.S. Effect of fuel to oxidant molar ratio on structural and dc electrical conductivity of ZnO nanoparticles prepared by simple solution combustion method. *J. Mater. Sci. Technol.* **2013**, *29*, 898–902. [[CrossRef](#)]
62. Deng, J.; Kang, L.; Bai, G.; Li, Y.; Li, P.; Liu, X.; Yang, Y.; Gao, F.; Liang, W. Solution combustion synthesis of cobalt oxides (Co₃O₄ and Co₃O₄/CoO) nanoparticles as supercapacitor electrode materials. *Electrochim. Acta* **2014**, *132*, 127–135. [[CrossRef](#)]
63. Biesinger, M.C.; Payne, B.P.; Grosvenor, A.P.; Lau, L.W.M.; Gerson, A.R.; Smart, R.S.C. Resolving surface chemical states in XPS analysis of first row transition metals, oxides and hydroxides: Cr, Mn, Fe, Co and Ni. *Appl. Surf. Sci.* **2011**, *257*, 2717–2730. [[CrossRef](#)]
64. Biesinger, M.C.; Payne, B.P.; Lau, L.W.M.; Gerson, A.; Smart, R.S.C. X-ray photoelectron spectroscopic chemical state Quantification of mixed nickel metal, oxide and hydroxide systems. *Surf. Interface Anal.* **2009**, *41*, 324–332. [[CrossRef](#)]
65. Payne, B.P.; Biesinger, M.C.; McIntyre, N.S. Use of oxygen/nickel ratios in the XPS characterisation of oxide phases on nickel metal and nickel alloy surfaces. *J. Electron Spectros. Relat. Phenomena* **2012**, *185*, 159–166. [[CrossRef](#)]
66. Grosvenor, A.P.; Biesinger, M.C.; Smart, R.S.C.; McIntyre, N.S. New interpretations of XPS spectra of nickel metal and oxides. *Surf. Sci.* **2006**, *600*, 1771–1779. [[CrossRef](#)]
67. Duan, X.; Pan, M.; Yu, F.; Yuan, D. Synthesis, structure and optical properties of CoAl₂O₄ spinel nanocrystals. *J. Alloys Compd.* **2011**, *509*, 1079–1083. [[CrossRef](#)]
68. Han, J.K.; Jia, L.T.; Hou, B.; Li, D.B.; Liu, Y.; Liu, Y.C. Catalytic properties of CoAl₂O₄/Al₂O₃ supported cobalt catalysts for Fischer-Tropsch synthesis. *J. Fuel Chem. Technol.* **2015**, *43*, 846–851. [[CrossRef](#)]
69. Biesinger, M.C.; Lau, L.W.M.; Gerson, A.R.; Smart, R.S.C. Resolving surface chemical states in XPS analysis of first row transition metals, oxides and hydroxides: Sc, Ti, V, Cu and Zn. *Appl. Surf. Sci.* **2010**, *257*, 887–898. [[CrossRef](#)]
70. Fu, L.; Yang, H. Tailoring the electronic structure of mesoporous spinel γ -Al₂O₃ at atomic level: Cu-doped case. *J. Phys. Chem. C* **2014**, *118*, 14299–14315. [[CrossRef](#)]
71. Biesinger, M.C. Advanced analysis of copper X-ray photoelectron spectra. *Surf. Interface Anal.* **2017**, *49*, 1325–1334. [[CrossRef](#)]
72. Thirumalairajan, S.; Mastelaro, V.R.; Escanhoela, C.A. In-depth understanding of the relation between CuAlO₂ particle size and morphology for ozone gas sensor detection at a nanoscale level. *ACS Appl. Mater. Interfaces* **2014**, *6*, 21739–21749. [[CrossRef](#)]

73. Xiong, D.; Zeng, X.; Zhang, W.; Wang, H.; Zhao, X.; Chen, W.; Cheng, Y.B. Synthesis and characterization of CuAlO₂ and AgAlO₂ delafossite oxides through low-temperature hydrothermal methods. *Inorg. Chem.* **2014**, *53*, 4106–4116. [[CrossRef](#)]
74. Pierron, E.D.; Rashkin, J.A.; Roth, J.F. Copper oxide on alumina. I. XRD studies of catalyst composition during air oxidation of carbon monoxide. *J. Catal.* **1967**, *9*, 38–44. [[CrossRef](#)]
75. Luo, M.F.; Fang, P.; He, M.; Xie, Y.L. In situ XRD, Raman, and TPR studies of CuO/Al₂O₃ catalysts for CO oxidation. *J. Mol. Catal. A Chem.* **2005**, *239*, 243–248. [[CrossRef](#)]
76. Renuka, N.K.; Shijina, A.V.; Praveen, A.K. Synthesis, characterisation, and CO oxidation activity of M/Al₂O₃ meso phase catalysts (M = Ce, V, Cu). *Mater. Lett.* **2013**, *113*, 96–99. [[CrossRef](#)]
77. Severino, F.; Brito, J.; Carías, O.; Laine, J. Comparative study of alumina-supported CuO and CuCr₂O₄ as catalysts for CO oxidation. *J. Catal.* **1986**, *102*, 172–179. [[CrossRef](#)]
78. Jiang, X.Y.; Zhou, R.X.; Pan, P.; Zhu, B.; Yuan, X.X.; Zheng, X.M. Effect of the addition of La₂O₃ on TPR and TPD of CuO/γ-Al₂O₃ catalysts. *Appl. Catal. A Gen.* **1997**, *150*, 131–141. [[CrossRef](#)]
79. Törnrcrona, A.; Skoglundh, M.; Thormählen, P.; Fridell, E.; Jobson, E. Low temperature catalytic activity of cobalt oxide and ceria promoted Pt and Pd: -influence of pretreatment and gas composition. *Appl. Catal. B Environ.* **1997**, *14*, 131–145. [[CrossRef](#)]
80. Thormählen, P.; Skoglundh, M.; Fridell, E.; Andersson, B. Low-temperature CO oxidation over platinum and cobalt oxide catalysts. *J. Catal.* **1999**, *188*, 300–310.
81. Jansson, J. Low-temperature CO oxidation over Co₃O₄/Al₂O₃. *J. Catal.* **2000**, *194*, 55–60. [[CrossRef](#)]
82. Wang, C.B.; Tang, C.W.; Tsai, H.C.; Kuo, M.C.; Chien, S.H. In situ FT-IR spectroscopic studies on the mechanism of the catalytic oxidation of carbon monoxide over supported cobalt catalysts. *Catal. Lett.* **2006**, *107*, 31–37. [[CrossRef](#)]
83. El-Shobaky, G.A.; Al-Noaimi, A.N. Catalytic oxidation of CO on sodium-treated NiO/Al₂O₃ solid. *Appl. Catal.* **1987**, *29*, 235–242. [[CrossRef](#)]
84. El-Shobaky, G.A.; El-Nabarawy, T.; Morsi, I.M.; Ghoneim, N.M. Physicochemical properties of NiO-Al₂O₃ mixed oxides and their relationship with thermal treatment and chemical composition. *Surf. Technol.* **1983**, *19*, 109–118.
85. El-Shobaky, G.A.; Al Noaimi, A.N. Surface properties of Ni-Al mixed oxide catalysts. *Surf. Technol.* **1985**, *26*, 235–244. [[CrossRef](#)]
86. Chen, C.S.; You, J.H.; Lin, J.H.; Chen, C.R.; Lin, K.M. The effect of a nickel promoter on the reducibility of a commercial Cu/ZnO/Al₂O₃ catalyst for CO oxidation. *Catal. Commun.* **2008**, *9*, 1230–1234. [[CrossRef](#)]



© 2020 by the authors. Licensee MDPI, Basel, Switzerland. This article is an open access article distributed under the terms and conditions of the Creative Commons Attribution (CC BY) license (<http://creativecommons.org/licenses/by/4.0/>).